PRIFYSGOL ABERYSTWYTH UNIVERSITY

Aberystwyth University

High-resolution mapping of losses and gains of Earth's tidal wetlands

Murray, Nicholas; Worthington, Thomas A.; Bunting, Pete; Duce, Stephanie; Hagger, Valerie; Lovelock, Catherine E.; Lucas, Richard; Saunders, Megan; Sheaves, Marcus; Spalding, Mark; Waltham, Nathan ; Lyons, Mitchell

Published in:
Science

DOI:
10.1126/science.abm9583
10.5281/zenodo.6503080
10.5281/zenodo.5968865
10.6084/m9.figshare.19121660.v2

Publication date:
2022

Citation for published version (APA):
Murray, N., Worthington, T. A., Bunting, P., Duce, S., Hagger, V., Lovelock, C. E., Lucas, R., Saunders, M., Sheaves, M., Spalding, M., Waltham, N., & Lyons, M. (2022). High-resolution mapping of losses and gains of Earth's tidal wetlands. *Science*, *376*(6594), 744-749. https://doi.org/10.1126/science.abm9583, https://doi.org/10.5281/zenodo.6503080, https://doi.org/10.5281/zenodo.5968865, https://doi.org/10.6084/m9.figshare.19121660.v2

Document License
CC BY

General rights
Copyright and moral rights for the publications made accessible in the Aberystwyth Research Portal (the Institutional Repository) are retained by the authors and/or other copyright owners and it is a condition of accessing publications that users recognise and abide by the legal requirements associated with these rights.

• Users may download and print one copy of any publication from the Aberystwyth Research Portal for the purpose of private study or research.
• You may not further distribute the material or use it for any profit-making activity or commercial gain
• You may freely distribute the URL identifying the publication in the Aberystwyth Research Portal

Take down policy
If you believe that this document breaches copyright please contact us providing details, and we will remove access to the work immediately and investigate your claim.

tel: +44 1970 62 2400
email: is@aber.ac.uk

Download date: 04. Nov. 2026

Title: High-resolution mapping of losses and gains of Earth's tidal wetlands

Authors: Nicholas J. Murray[1]*, Thomas A. Worthington[2], Pete Bunting[3], Stephanie Duce[1], Valerie Hagger[4], Catherine E. Lovelock[4], Richard Lucas[3], Megan I. Saunders[5], Marcus Sheaves[1], Mark Spalding[6], Nathan J. Waltham[1,7], Mitchell B. Lyons[8]

Affiliations:

[1]College of Science and Engineering, James Cook University; Townsville, Australia.

[2]Conservation Science Group, Department of Zoology, University of Cambridge; Cambridge, UK.

[3]Department of Geography and Earth Sciences, Aberystwyth University; Aberystwyth, Wales, UK.

[4]School of Biological Sciences, The University of Queensland; Brisbane, Australia.

[5] Coasts and Ocean Research Program, CSIRO Oceans and Atmosphere; St Lucia, Australia.

[6]The Nature Conservancy, Department of Physical, Earth, and Environmental Sciences, University of Siena; Siena, Italy.

[7]TropWATER, Centre for Tropical Water and Aquatic Ecosystem Research, James Cook University; Townsville, Australia.

[8]Centre for Ecosystem Science, School of Biological, Earth and Environmental Sciences, University of New South Wales; Sydney, Australia.

*Corresponding author. Email: nicholas.murray@jcu.edu.au

Abstract: Tidal wetlands are expected to respond dynamically to global environmental change, but the extent to which wetland losses have been offset by gains remains poorly understood. We developed a global analysis of satellite data to simultaneously monitor change of three highly interconnected intertidal ecosystem types—tidal flats, tidal marshes and mangroves—from 1999 to 2019. Globally, 13,700 km^2 of tidal wetlands were lost, but these have been substantially offset by gains of 9,700 km^2, leading to a net change of −4000km^2 over two-decades. We found 27% of losses and gains were associated with direct human activities, such as conversion to agriculture and restoration of lost wetlands. All other changes were attributed to indirect drivers including the combined effects of natural coastal processes and climate change.

One-Sentence Summary: High-resolution satellite analysis quantifies the global dynamics of tidal wetlands.

Main Text:

Tidal wetlands are of immense importance to humanity, providing benefits such as carbon storage and sequestration, coastal protection, and fisheries enhancement (*1*, *2*). Unfortunately, intensifying anthropogenic pressures and the growing impacts of climate change are affecting tidal wetlands and their component intertidal ecosystems in pervasive ways. Losses of tidal wetlands are widely reported (*3*-*5*), yet at local scales intertidal ecosystems are known to have the capacity to respond to environmental change, gaining extent by means of sediment accumulation, inland migration and redistribution (*6*-*9*). Redistribution and recovery through natural processes are increasingly supplemented by broad-scale ecosystem restoration activities (*10*). Although a number of studies have suggested that intertidal ecosystems are highly resilient to environmental change (*11*, *12*), little is known about the degree to which gains in tidal wetland extent have counterbalanced known losses . Previous analyses have been unable to address this

question, owing to a focus on mapping single ecosystem types (*9, 13, 14*), which cannot distinguish losses from transitions among adjacent intertidal ecosystems, a lack of consistent data on the global extent and change of tidal marshes (*15*), and knowledge of the prevailing drivers of tidal wetland change. This has led to considerable uncertainty about how tidal wetlands have changed in recent decades and how they are expected to persist into the future (*11, 12*).

Here, we report on an integrated, globally consistent analysis of the distribution and change of Earth's three intertidal ecosystems: tidal flats, tidal marshes, and mangroves (hereafter referred to collectively as 'tidal wetlands'; Fig. S1). Where they co-occur, these three ecosystems are highly interconnected, with feedback mechanisms among biological and physical components that interact extensively across the systems (*8*). We investigate the spatiotemporal distribution of tidal wetlands globally by applying stacked machine-learning classifiers to remotely sensed data to model their occurrence, detect the type and timing of loss and gain events, and assess the drivers of change over the period 1999 to 2019. The validated dataset is produced by combining observations from 1,166,385 satellite images acquired by the Landsat 5-8 missions with environmental data of variables known to influence the distributions of each ecosystem type, including temperature, slope and elevation (Tables S1 and S2). Tidal wetland loss was defined as the replacement of any of the three focal ecosystems with non-intertidal ecosystems at the 30-m pixel scale, with tidal wetland gain defined as their establishment in pixels where they did not occur in 1999. A weighted random sample of detected changes was used to estimate the contribution of direct human impacts versus indirect drivers such as sea level rise and natural coastal processes on tidal wetland losses and gains globally (*16*).

Our global dataset reveals the total observed area of tidal wetlands in 2019 was at least 354,600 km^2 (95% confidence interval (CI): 244,800, 363,900 km^2). Tidal wetlands are unevenly

distributed across the world's coastlines, with the largest remaining contiguous tracts occurring as deltaic mangroves fringed by extensive tidal flats in the Amazon Delta, Northern Bay of Bengal, New Guinea, and the Niger Delta (Fig. 1A). Previous estimates of global tidal marsh extent rely on spatial data compilations with large gaps in coverage that lead to underestimates of extent (*15*), limiting their use for estimating global blue carbon stocks (*17*). Our data therefore allow a first empirical estimate of global tidal marsh extent of 90,800 km^2, obtained by subtracting previously derived extent estimates of mangroves (135,900 km^2) and tidal flats (127,900 km^2) from our global tidal wetland area estimate (*9, 18*). Our estimate of tidal marsh extent represents 25.6% of the total tidal wetland extent mapped in this study and is 65.1% greater than the previously reported minimum global estimate of 55,000 km^2 (*15*). Owing to limitations of our methods in regions higher than 60°N latitude, where tidal marshes and tidal flats are known to occur, this upward revision of global tidal marsh extent should be considered conservative.

Tracking change over the 20-year study period indicates that losses of 13,700 km^2 (95% CI: −16,800, −8,200 km^2) have been substantially offset by the establishment of 9,700 km^2 (95% CI: +4,900, +15,700 km^2) of new tidal wetlands that were not present in 1999 (Table 1). Despite wide geographic variation in the occurrence of tidal wetlands globally, many regions showed a consistent pattern of losses being substantially offset by nearby gains (Fig. 1, B-C). This pattern was most pronounced in the world's major river deltas (*19*), where about one-fifth (19.1%) of the area of tidal wetland changes occurred, despite containing only 7.5% of the world's tidal wetland extent (Fig. 2A). We recorded the greatest tidal wetland change in the Ganges-Brahmaputra (1,070 km^2) and Amazon deltas (730 km^2), both of which have increased tidal wetland extent since 1999 (ratio of loss to gain 0.92 and 0.98, respectively). Many deltas have experienced a net

increase in total extent over the past three decades due to increases in fluvial sediment supply caused by catchment deforestation and increased upland soil erosion (*19*). Our data, however, suggest a net loss of tidal wetlands on deltas globally, though gains of 2,100 km^2 alongside losses of −2,300 km^2 indicate the considerable dynamism of these systems. The latter have been associated with multiple direct drivers of change such as conversion to agriculture and aquaculture (*9, 14*), urban expansion (*20*), and geomorphic changes due to dikes and channel diversions (*20*), together with many indirect drivers including shoreline erosion (*9, 20*), compaction, subsidence and sea level rise (*21*), storm driven vegetation loss (*22*), pollution (*23*), and altered sediment supply (*19*).

Of the three intertidal ecosystems included in the analysis, tidal flats experienced both the greatest loss (7,000 km^2; 95% CI: 4,200, 8,600 km^2) and gain (6,700 km^2; 95% CI: 3,400, 10,800km^2), accounting for almost two-thirds (58.8%) of the total tidal wetland area change (Table 1; Fig. 3A). A ratio of loss to gain of 1.1 indicates that newly established tidal flats have made a substantial contribution to offsetting the magnitude of their net loss globally. By contrast, mangroves had the highest ratio of loss to gain (3.0), with an estimated net decrease in extent of 3,700 km^2 (95% CI: −5,400, −2,100 km^2), indicating extensive mangrove losses have only been partially offset by the 1,800 km^2 (95% CI: +900, +3,000 km^2) of new mangroves detected by our analysis. Tidal marshes had the lowest total area change and were the only ecosystem to have a loss to gain ratio of <1, indicating that their gain marginally exceeded their loss for an estimated net increase of 100 km^2 (95% CI: 0, +100 km^2). Our estimates of global tidal wetland change partitioned by ecosystem type agree in magnitude with recently published estimates of mangrove change from 2000 to 2016 of −3,400 km^2 (*14*). No comparable global estimates of tidal flats and

tidal marsh change are available due to differing coverage of change analyses of tidal flats (*9*) and a lack of any data sufficient to support global change analyses of tidal marshes (*15*).

About three-quarters of the 4,000 km^2 net global tidal wetland decrease between 1999 and 2019 occurred in Asia (74.1%), with 68.6% concentrated in just three countries: Indonesia (36%), China (20.6%) and Myanmar (12%). Losses of tropical mangrove forests across Southeastern Asia, particularly Indonesia and Myanmar, are well-documented (*14*, *18*), and the extensive impact of coastal land conversion was confirmed by our analysis (Fig. 3B). There was also a large net reduction of tidal flat extent in China of more than 1,000 km^2 largely due to reclamation (*24*), but net gains of tidal marshes (+ 200 km^2) that coincide with the rapid expansion of *Spartina alterniflora* across China's intertidal zone (Fig. 3C; *25*) reduced China's net tidal wetland loss to 800 km^2 (Table S3). Outside of Asia, tidal wetlands in Africa had the highest ratio of loss to gain (1.6), indicating a strong loss dynamic that has been associated with severe mangrove degradation, which is most intense in Nigeria, Mozambique and Guinea-Bissau (Fig. 1B; Table S3).

Interpretation of a globally distributed random sample of tidal wetland losses and gains suggested that 39% of losses and 14% of gains were caused by direct human activities (Table S9). Direct human activities were defined as observable activities occurring at the location of the detected change (*26*), including conversion to aquaculture, agriculture, plantations, coastal developments and other physical structures such as the building of seawalls and dikes (*9*) (Fig. S8). They also include drivers of gain such as mangrove planting, restoration activities or coastal modifications to promote tidal exchange (Fig. 2B; Fig. S8).

At the continental scale, Asia was identified as the global center of tidal wetland loss from direct human activities (Fig. S9). In Asia, direct drivers accounted for more than two-thirds of

the losses of each ecosystem (mangrove, 75%; tidal marsh, 69%; tidal flats; 62%; Table S10), confirming the negative effects of widespread coastal transformation on coastal ecosystems. Although the impact of coastal development on mangroves and tidal wetlands have been previously reported (*9, 14*), our results reveal that Asian tidal marshes have similarly been severely degraded by human activities. Compared with Asia, direct human activities had a much lesser role in the losses of tidal wetlands in Europe (28%), Africa (27%), North America (9%), South America (2%) and Oceania (0%; Fig. S9).

Indirect or ex situ drivers include both natural coastal processes and those influenced by human activities remotely from the location of observed change. They include processes of isostatic change (*21*), sea level rise (*8*), storm impacts (*22*), erosion and progradation (*22*), along-shore coastal development (*9*), and their combined effects. More than 90% of tidal wetland losses in North America (91%), South America (98%) and Oceania (100%) were attributed to indirect drivers (Fig. S9). Globally, indirect drivers accounted for most losses of tidal marsh (78%) and tidal flats (66%), whereas mangrove losses were equally a result of direct and indirect drivers (50%; Table S9).

Most tidal wetland gains (86%) were the result of indirect drivers, highlighting the prominent role that broad-scale coastal processes have in controlling tidal wetland extent and facilitating natural regeneration. However, disentangling the specific processes underpinning drivers is challenging with analyses conducted at large-spatial scales. In most cases direct drivers could be clearly identified, but many indirect drivers operate over large spatial and temporal scales and may originate tens to thousands of kilometers from an observed tidal wetland change. Change in ecosystem extent can also be the result of more than one indirect driver or of interactions between drivers. Our work therefore suggests a need for continued monitoring,

experiments and models that can account for these complexities to help characterize and predict global tidal wetland dynamics.

There is potential to use our analysis, which is designed to be periodically updated, to track larger-scale coastal ecosystem restoration activities. While there has been a surge in coastal restoration efforts worldwide (*27*), many of these fail (*10*). Monitoring progress of restoration remotely, independently, and at broad-scales could contribute to reporting on international conservation initiatives such as the UN Decade on Ecosystem Restoration, on targets associated with the Convention on Biological Diversity, and on mitigation commitments made under the UN Framework Convention on Climate Change (*27*). The driver analysis indicated that 14% of observed tidal wetland gains were attributable to direct human interventions (Table S9). These activities were most apparent for tidal marshes and were typically the product of site scale restoration activities (Fig. 2B; Fig. S8).

Our analysis enables the detection and characterization of dynamic transitions among intertidal ecosystem types globally. Transitions have been linked to a number of physical and climatic factors, such as sea level rise, geomorphic changes, and variation in temperature and rainfall (*28, 29*). We found that 1.9% of the world's tidal wetlands exhibited transitions among ecosystem types over the study period (6,700 km^2; Table S4). Transition events tended to be spatially clustered with areas of large losses and gains, and in many cases may be linked to the same drivers (*8*). Over 55% of transitions (>3,600km^2) were colonization of tidal flats by marsh or mangrove, with a further 27% being transitions from mangrove to tidal marsh or vice versa (Table S4).

Our classifier accurately detected known events of coastal change across the three ecosystem types. For example, the magnitude 9.2 Aceh-Andaman earthquake on 26 December 2004 caused

up to 2.9m of tectonic subsidence in the Andaman and Nicobar Islands, leading to land submergence and a >90% loss of mangrove extent in some localities (Fig. 2C; *30*). However, as for all earth observation-derived estimates of land cover change, there are limitations. These include the spatial resolution of sensor data, which limit the ability of our analysis to detect change in narrow linear features such as waterways; model uncertainty; errors of omission and commission; and a lack of polar coverage. Validation of our data products was effective in characterizing these uncertainties, which were propagated through our estimates of tidal wetland extent and change (Tables S5 to S8).

By simultaneously mapping three of Earth's intertidal ecosystems, this work enables a synoptic view of change of three of the world's highly connected intertidal coastal ecosystems. This approach offers an advantage over single-ecosystem mapping studies, as short- and long-term dynamic transitions between ecosystem types can cause considerable apparent change in individual ecosystems. While our study is unable to account for the impact of centuries of anthropogenic coastal transformation and related pressures (*8*), it has established an observational record of recent tidal wetland changes with preliminary attribution of change drivers. Such information has the potential to promote objective monitoring of conservation and restoration efforts, assess the impacts of elevating pressures, guide new studies of changing ecosystem structure, function and service provision in newly established tidal wetlands (*8*, *29*), and improve our understanding of the resilience of tidal wetlands in the face of global change. In turn, it can support efforts to anticipate the future of the global coastal environment and to develop adaptive responses to change.

References and Notes

1. E. B. Barbier *et al.*, The value of estuarine and coastal ecosystem services. *Ecol. Monogr.* **81**, 169-193 (2011).
2. M. D. Spalding *et al.*, Coastal ecosystems: a critical element of risk reduction. *Conservation Letters* **7**, 293-301 (2014).
3. E. B. Barbier, A global strategy for protecting vulnerable coastal populations. *Science* **345**, 1250-1251 (2014).
4. D. A. Friess *et al.*, The state of the world's mangrove forests: past, present, and future. *Annual Review of Environment and Resources* **44**, 89-115 (2019).
5. D. M. FitzGerald, Z. Hughes, Marsh Processes and Their Response to Climate Change and Sea-Level Rise. *Annu Rev Earth Pl Sc* **47**, 481-517 (2019).
6. C. E. Lovelock *et al.*, The vulnerability of Indo-Pacific mangrove forests to sea-level rise. *Nature* **526**, 559-563 (2015).
7. S. Fagherazzi *et al.*, Numerical models of salt marsh evolution: Ecological, geomorphic, and climatic factors. *Rev. Geophys.* **50**, RG1002 (2012).
8. M. L. Kirwan, J. P. Megonigal, Tidal wetland stability in the face of human impacts and sea-level rise. *Nature* **504**, 53-60 (2013).
9. N. J. Murray *et al.*, The global distribution and trajectory of tidal flats. *Nature* **565**, 222-225 (2019).
10. E. Bayraktarov *et al.*, The cost and feasibility of marine coastal restoration. *Ecol. Appl.* **26**, 1055-1074 (2016).

11. M. L. Kirwan, S. Temmerman, E. E. Skeehan, G. R. Guntenspergen, S. Fagherazzi, Overestimation of marsh vulnerability to sea level rise. *Nature Climate Change* **6**, 253-260 (2016).

12. M. Schuerch *et al.*, Future response of global coastal wetlands to sea-level rise. *Nature* **561**, 231-234 (2018).

13. P. Bunting *et al.*, The Global Mangrove Watch—A new 2010 global baseline of mangrove extent. *Remote Sensing* **10**, 1669 (2018).

14. L. Goldberg, D. Lagomasino, N. Thomas, T. Fatoyinbo, Global declines in human-driven mangrove loss. *Glob Chang Biol* **26**, 5844-5855 (2020).

15. C. Mcowen *et al.*, A global map of saltmarshes. *Biodiversity Data Journal* **5**, e11764 (2017).

16. Materials and methods are available as supplementary materials.

17. P. I. Macreadie *et al.*, The future of Blue Carbon science. *Nat. Commun.* **10**, 3998 (2019).

18. M. Spalding, M. Leal, "The state of the world's mangroves 2021," (Global Mangrove Alliance, 2021).

19. J. H. Nienhuis *et al.*, Global-scale human impact on delta morphology has led to net land area gain. *Nature* **577**, 514-518 (2020).

20. K. B. Gedan, B. R. Silliman, M. D. Bertness, Centuries of human-driven change in salt marsh ecosystems. *Annual Review of Marine Science* **1**, 117-141 (2009).

21. J. P. M. Syvitski *et al.*, Sinking deltas due to human activities. *Nature Geoscience* **2**, 681-686 (2009).

22. D. Lagomasino *et al.*, Storm surge and ponding explain mangrove dieback in southwest Florida following Hurricane Irma. *Nat. Commun.* **12**, 4003 (2021).

23. L. A. Deegan *et al.*, Coastal eutrophication as a driver of salt marsh loss. *Nature* **490**, 388-392 (2012).

24. X. Wang *et al.*, Rebound in China's coastal wetlands following conservation and restoration. *Nature Sustainability*, **4**, 1076–1083 (2021).

25. M. Liu *et al.*, Rapid invasion of *Spartina alterniflora* in the coastal zone of mainland China: new observations from Landsat OLI images. *Remote Sensing* **10**, 1933 (2018).

26. X.-P. Song *et al.*, Global land change from 1982 to 2016. *Nature* **560**, 639-643 (2018).

27. C. M. Duarte *et al.*, Rebuilding marine life. *Nature* **580**, 39-51 (2020).

28. K. C. Cavanaugh *et al.*, Climate-driven regime shifts in a mangrove–salt marsh ecotone over the past 250 years. *Proc. Natl. Acad. Sci. U. S. A.* **116**, 21602-21608 (2019).

29. N. Saintilan *et al.*, Thresholds of mangrove survival under rapid sea level rise. *Science* **368**, 1118-1121 (2020).

30. P. Nehru, P. Balasubramanian, Mangrove species diversity and composition in the successional habitats of Nicobar Islands, India: A post-tsunami and subsidence scenario. *Forest Ecology and Management* **427**, 70-77 (2018).

31. S. K. Hong *et al.*, Land use in Korean tidal wetlands: impacts and management strategies. *Environ. Manage.* **45**, 1014-1026 (2010).

32. D. Keith *et al.*, "The IUCN Global Ecosystem Typology v2.0: Descriptive profiles for Biomes and Ecosystem Functional Groups," (The International Union for the Conservation of Nature (IUCN), Gland, 2020).

33. M. J. Bishop, N. J. Murray, S. Swearer, D. A. Keith, in *The IUCN Global Ecosystem Typology 2.0: Descriptive profiles for biomes and ecosystem functional groups*, D. A.

Keith, J. R. Ferrer-Paris, E. Nicholson, R. T. Kingsford, Eds. (IUCN, Gland, Switzerland, 2020).

34. D. A. Keith, A. H. Altieri, J. Loidi, M. J. Bishop, in *The IUCN Global Ecosystem Typology 2.0: Descriptive profiles for biomes and ecosystem functional groups*, D. A. Keith, J. R. Ferrer-Paris, E. Nicholson, R. T. Kingsford, Eds. (IUCN, Gland, Switzerland, 2020).

35. M. J. Bishop, A. H. Altieri, T. S. Bianchi, D. A. Keith, in *The IUCN Global Ecosystem Typology 2.0: Descriptive profiles for biomes and ecosystem functional groups*, D. A. Keith, J. R. Ferrer-Paris, E. Nicholson, R. T. Kingsford, Eds. (IUCN, Gland, Switzerland, 2020).

36. L. Breiman, Random forests. *Machine learning* **45**, 5-32 (2001).

37. C. Amante, B. W. Eakins, *ETOPO1 1 arc-minute global relief model: procedures, data sources and analysis*. (US Department of Commerce, National Oceanic and Atmospheric Administration, National Environmental Satellite, Data, and Information Service, National Geophysical Data Center, Marine Geology and Geophysics Division, 2009).

38. T. A. Worthington *et al.*, A global typology of mangroves and its relevance for ecosystem services and deforestation. *Scientific reports*, **10**, 14652 (2020).

39. C. Giri *et al.*, Status and distribution of mangrove forests of the world using earth observation satellite data. *Global Ecology and Biogeography* **20**, 154-159 (2011).

40. Natural Earth Data. Coastline. (Available online at https://www.naturalearthdata.com/downloads/10m-physical-vectors/10m-coastline, 2020).

41. N. Gorelick *et al.*, Google Earth Engine: Planetary-scale geospatial analysis for everyone. *Remote Sens. Environ.* **202**, 18-27 (2017).

42. R Core Team. (R Foundation for Statistical Computing, Vienna, Austria., 2020).

43. M. C. Hansen, T. R. Loveland, A review of large area monitoring of land cover change using Landsat data. *Remote Sens. Environ.* **122**, 66-74 (2012).

44. R. E. Kennedy *et al.*, Bringing an ecological view of change to Landsat-based remote sensing. *Fron. Ecol. Environ.* **12**, 339-346 (2014).

45. N. J. Murray *et al.*, The role of satellite remote sensing in structured ecosystem risk assessments. *Sci Total Environ* **619-620**, 249-257 (2018).

46. US Geological Survey, "Landsat 4-7 Collection 1 (C1) Surface Reflectance (LEDAPS) Product Guide. Version 3.0," (USGS, 2020).

47. P. V. Potapov *et al.*, Quantifying forest cover loss in Democratic Republic of the Congo, 2000–2010, with Landsat ETM+ data. *Remote Sens. Environ.* **122**, 106-116 (2012).

48. M. C. Hansen *et al.*, High-resolution global maps of 21st-century forest cover change. *Science* **342**, 850-853 (2013).

49. G. Azzari, D. B. Lobell, Landsat-based classification in the cloud: An opportunity for a paradigm shift in land cover monitoring. *Remote Sens. Environ.* **202**, 64-74 (2017).

50. V. Kovalskyy, D. P. Roy, The global availability of Landsat 5 TM and Landsat 7 ETM+ land surface observations and implications for global 30m Landsat data product generation. *Remote Sens. Environ.* **130**, 280-293 (2013).

51. N. Saintilan, N. C. Wilson, K. Rogers, A. Rajkaran, K. W. Krauss, Mangrove expansion and salt marsh decline at mangrove poleward limits. *Glob Chang Biol* **20**, 147-157 (2014).

52. J. Takaku, T. Tadono, K. Tsutsui, Generation of high resolution global DSM from ALOS PRISM. *ISPRS Annals of Photogrammetry, Remote Sensing & Spatial Information Sciences* **2**, 243-248 (2014).

53. M. N. Wright, A. Ziegler, ranger: A Fast Implementation of Random Forests for High Dimensional Data in C++ and R. *Journal of Statistical Software* **77**, 1 - 17 (2017).

54. J. R. Eastman, J. Toledano, "Phase 3 Extension to the Mapping of Tropical Pond Aquaculture, Mangroves and Coastal Wetlands," *Aquaculture and Coastal Habitats Report No. 6* (Clark Labs, 2020).

55. R. M. Fuller, G. M. Smith, B. J. Devereux, The characterisation and measurement of land cover change through remote sensing: problems in operational applications? *Int J App Earth Obs Geo* **4**, 243-253 (2003).

56. C. K. F. Lee, E. Nicholson, C. Duncan, N. J. Murray, Estimating changes and trends in ecosystem extent with dense time-series satellite remote sensing. *Conserv Biol* **35**, 325-335 (2021).

57. P. Olofsson *et al.*, Good practices for estimating area and assessing accuracy of land change. *Remote Sens. Environ.* **148**, 42-57 (2014).

58. M. C. Hansen, P. Potapov, A. Tyukavina, Comment on “Tropical forests are a net carbon source based on aboveground measurements of gain and loss”. *Science* **363**, eaar3629 (2019).

59. R. G. Congalton, K. Green, *Assessing the Accuracy of Remotely Sensed Data: Principles and Practices*. (CRC press, 2008).

60. R. Congalton, J. Gu, K. Yadav, P. Thenkabail, M. Ozdogan, Global Land Cover Mapping: A Review and Uncertainty Analysis. *Remote Sensing* **6**, 12070-12093 (2014).

61. P. Olofsson, G. M. Foody, S. V. Stehman, C. E. Woodcock, Making better use of accuracy data in land change studies: Estimating accuracy and area and quantifying uncertainty using stratified estimation. *Remote Sens. Environ.* **129**, 122-131 (2013).

62. S. V. Stehman, J. D. Wickham, Assessing accuracy of net change derived from land cover maps. *Photogrammetric Engineering & Remote Sensing* **72**, 175-185 (2006).

63. B. Efron, R. Tibshirani, Improvements on cross-validation: the 632+ bootstrap method. *Journal of the American Statistical Association* **92**, 548-560 (1997).

64. S. K. McFeeters, The use of the Normalized Difference Water Index (NDWI) in the delineation of open water features. *Int. J. Remote Sens.* **17**, 1425-1432 (1996).

65. H. Xu, Modification of normalised difference water index (NDWI) to enhance open water features in remotely sensed imagery. *Int. J. Remote Sens.* **27**, 3025-3033 (2006).

66. G. L. Feyisa, H. Meilby, R. Fensholt, S. R. Proud, Automated Water Extraction Index: A new technique for surface water mapping using Landsat imagery. *Remote Sens. Environ.* **140**, 23-35 (2014).

67. M. B. Lyons, D. A. Keith, S. R. Phinn, T. J. Mason, J. Elith, A comparison of resampling methods for remote sensing classification and accuracy assessment. *Remote Sens. Environ.* **208**, 145-153 (2018).

68. G. P. Asner *et al.*, Selective logging in the Brazilian Amazon. *Science* **310**, 480-482 (2005).

69. Flanders Marine Institute. Union of the ESRI Country shapefile and the Exclusive Economic Zones (version 3) (Available online at https://doi.org/10.14284/403 , 2020).

70. M. D. Spalding et al., Marine ecoregions of the world: A bioregionalization of coastal and shelf areas. *Bioscience* 57, 573-583 (2007).

71. D. R. Richards, D. A. Friess, Rates and drivers of mangrove deforestation in Southeast Asia, 2000–2012. *Proc. Natl. Acad. Sci. U. S. A.* **113**, 344-349 (2016).

72. J. Franklin, J. M. Serra-Diaz, A. D. Syphard, H. M. Regan, Global change and terrestrial plant community dynamics. *Proc. Natl. Acad. Sci. U. S. A.*, 113, 3725-3734 (2016).

Acknowledgments: We thank R. Canto, M. Toor and N. Younes Cárdenas for assistance with developing the training data. Landsat data are courtesy of NASA Goddard Space Flight Center and U.S. Geological Survey. We thank the Google Earth Engine team for providing Earth Engine, and Michael Dewitt and Nick Clinton for assistance with processing Landsat covariates in Earth Engine.

Funding:

Australian Research Council Discovery Early Career Research Award DE190100101 (N.J.M.);

Australian Research Council Discovery Australian Laureate Fellowship FL200100133 (C.E.L.)

Julius Career Award from CSIRO (M.I.S.)

Australian Research Council Linkage grant LP170101171 (V.H.)

Author contributions:

Conceptualization: NJM, TAW, MBL

Data curation: NJM, TAW

Methodology: NJM, TAW, MBL, CEL, VH, MIS

Formal Analysis: NJM, TAW, MBL, SD

Funding acquisition: NJM

Writing – original draft: NJM, TAW, MBL

Writing – review & editing: All authors.

Competing interests: Authors declare that they have no competing interests.

Data and materials availability: Code to develop the global tidal wetland change product is available at Zenodo (10.5281/zenodo.5968865). Global tidal wetland training data is available at Figshare (10.6084/m9.figshare.19121660). The tidal wetland data products are viewable at www.globalintertidalchange.org and made available in several formats via Zenodo (10.5281/zenodo.5989203). Landsat Archive data are freely available courtesy of the U.S. Geological Survey (https://www.usgs.gov/landsat-missions/landsat-collection-1) and via Google Earth Engine Data Catalog (https://developers.google.com/earth-engine/datasets/catalog/landsat).

Supplementary Materials

Materials and Methods

Figs. S1 to S9

Tables S1 to S10

References (*31*–*72*)

Table 1. Tidal wetland change estimates by intertidal ecosystem type for different regions of the world from 1999 to 2019. Change estimates are in square kilometers. Tidal wetlands in this study collectively refer to tidal flat, tidal marsh and mangrove ecosystems, such that area change of tidal wetlands is the sum of the change area of the three component intertidal ecosystems. Per-pixel loss and gain were summed to estimate loss and gain area of tidal wetlands and their component ecosystem types at these regional scales, with 95% confidence intervals derived from quantitative accuracy assessment in brackets. Analysis units are realms from the Marine Ecoregions of the World.

Marine Ecoregion Realm	Tidal flat		Mangrove		Tidal marsh		Tidal wetlands	
	Loss	Gain	Loss	Gain	Loss	Gain	Loss	Gain
Central Indo-Pacific	-952 (-1169,-570)	1156 (589,1871)	-2719 (-3338,-1626)	758 (387,1227)	-12 (-15,-7)	7 (4,12)	-3683 (-4522,-2203)	1921 (980,31
Western Indo-Pacific	-1573 (-1932,-941)	1741 (888,2818)	-1139 (-1398,-681)	380 (194,616)	-18 (-22,-11)	66 (34,107)	-2730 (-3351,-1633)	2187 (1115,35
Tropical Atlantic	-1067 (-1309,-638)	1082 (552,1752)	-1541 (-1892,-922)	567 (289,919)	-14 (-18,-9)	5 (2,8)	-2622 (-3219,-1569)	1654 (844,26
Temperate Northern Pacific	-2355 (-2891,-1408)	1415 (722,2291)	-31 (-38,-18)	26 (13,43)	-192 (-236,-115)	428 (218,693)	-2578 (-3165,-1542)	1869 (954,30
Temperate Northern Atlantic	-594 (-729,-355)	827 (422,1338)	-2 (-2,-1)	2 (1,3)	-680 (-835,-407)	478 (244,774)	-1276 (-1566,-763)	1307 (667,21
Tropical Eastern Pacific	-106 (-131,-64)	110 (56,178)	-93 (-115,-56)	86 (44,139)	0 (0,0)	0 (0,1)	-200 (-246,-120)	196 (100,31
Temperate South America	-110 (-135,-66)	117 (60,190)	-4 (-5,-2)	5 (3,8)	-66 (-82,-40)	111 (57,180)	-181 (-222,-108)	233 (119,37
Arctic	-118 (-145,-71)	173 (88,280)	0 (0,0)	0 (0,0)	-30 (-36,-18)	36 (19,59)	-148 (-182,-88)	209 (107,33
Temperate Australasia	-86 (-105,-51)	66 (34,107)	-13 (-16,-8)	2 (1,2)	-43 (-53,-26)	20 (10,32)	-141 (-174,-85)	87 (44,14
Eastern Indo-Pacific	-53 (-65,-32)	4 (2,7)	-1 (-1,-1)	1 (0,1)	0 (0,0)	0 (0,0)	-54 (-67,-33)	5 (3,8)
Temperate Southern Africa	-9 (-11,-5)	8 (4,13)	-19 (-23,-11)	1 (0,1)	-6 (-7,-4)	11 (6,18)	-33 (-41,-20)	20 (10,32
Southern Ocean	-4 (-5,-3)	2 (1,4)	0 (0,0)	0 (0,0)	-1 (-1,-1)	1 (1,2)	-5 (-6,-3)	4 (2,6)
Total	-7028 (-8628,-4204)	6700 (3418,10849)	-5561 (-3326,-6827)	1828 (932,2960)	-1064 (-1306,- 636)	1164 (594,1884)	-13652 (-16760,-8166)	9692 (4944,15

Fig. 1. The global distribution of major tidal wetlands and their change from 1999 to 2019. (**A**) The 2019 distribution of tidal wetlands is modeled as the combined distribution of the world's three main intertidal ecosystems, tidal flats, tidal marshes, and mangroves. Darker colors indicate greater area of tidal wetlands per 2° grid cell. (**B**) Losses, (**C**) gains over the period 1999 to 2019. Circle sizes indicate the extent of tidal wetland loss and gain over the study period in km^2 per 2° grid cell.

Fig. 2. Representative examples of 1999–2019 tidal wetland loss and gain. (**A**) Losses and gains of tidal flats and tidal marshes following diversion of the main channel in 1996, Yellow River delta, China (left). Reference images acquired 1998 (middle) and 2020 (right). (**B**) Tidal marsh gain due to Europe's largest coastal wetland restoration project, United Kingdom (left). Reference images acquired 1999 (middle) and 2018 (right). (**C**) Mangrove loss due to tectonic subsidence following the Aceh-Andaman earthquake of 2004, Katchal Island, Nicobar Islands (left). Reference images acquired 1992 (middle) and 2019 (right). Imagery data are from USGS (**A** and **C**) and Google Earth Pro (**B**). All scale bars are 5 km.

Fig. 3. Tidal wetland change totals from 1999 to 2019. Panels show the losses and gains of tidal wetlands per time step for (**A**) the global study area, (**B**) Indonesia and (**C**) China. Shaded colors represent intertidal ecosystem types mapped by this analysis. White lines indicate the net change of tidal wetlands. Note that area change cannot be estimated for the initial time step of the analysis (1999-2001).

Science
AAAS

Supplementary Materials for

Losses and gains of Earth's tidal wetlands

Nicholas J. Murray[1]*, Thomas A. Worthington[2], Pete Bunting[3], Stephanie Duce[1], Valerie Hagger[4], Catherine E. Lovelock[4], Richard Lucas[3], Megan I. Saunders[5], Marcus Sheaves[1], Mark Spalding[6], Nathan J. Waltham[1,7], Mitchell B. Lyons[8].

Correspondence to: nicholas.murray@jcu.edu.au

This PDF file includes:

Materials and Methods
Figs. S1 to S9
Tables S1 to S10

Materials and Methods

1. Overview

This study establishes a framework for mapping the distribution and change of the world's tidal wetlands with satellite image archives and biophysical data. Tidal wetlands in our study collectively refer to three of the world's most extensive intertidal ecosystem types: tidal flats, tidal marshes and mangroves (*8, 12, 31*). These three intertidal ecosystem types are regularly inundated throughout the tidal cycle correspond to the IUCN Global Ecosystem Typology (*32*) descriptions for muddy shorelines (typology code MT1.2; hereafter 'tidal flats'*)*, coastal tidal marshes and reedbeds (MFT1.3; hereafter 'tidal marshes') and intertidal forests and shrublands (MFT1.2; hereafter 'mangroves'). In this study tidal flats are represented as fine to coarse particle-sized sediment and sand dominated ecosystems that are regularly inundated throughout the tidal cycle and occur primarily on low-sloping, low energy coastlines (*9*, *33*), tidal marshes as salt-tolerant forbs, grasses and shrubs that occur in intertidal environments (*34*), and mangroves as structurally complex intertidal forests that occur mainly in warm regions (Figure S1) (*35*).

Vague distribution boundaries between intertidal ecosystems present a considerable challenge for remote sensing analyses of coastal ecosystems. Remote sensing studies can over- or under-estimate the extent of single ecosystems due to continuous ecotones among each ecosystem type, the occurrence of complex ecosystem mosaics at a range of spatial scales within the intertidal zone, variable vegetation height within vegetated coastal ecosystems, limited height development of tree species on some substrates, sparse vegetation cover, the dynamic movement of ecotones over time, and varying tidal inundation at the time of remote observation. These issues tend to result in gaps or overlaps in independently developed maps of coastal ecosystems, limiting their ability to be used for integrated analyses of global tidal wetland dynamics. To

address this, we developed a three-stage classification workflow for earth observation data that sought to (i) estimate the occurrence of the three intertidal ecosystems in a single map class ('tidal wetlands') for seven time-steps between 1999 and 2019 (Stage 1), (ii) detect and classify their change over the full 20-year study period (Stage 2), and (iii) classify tidal wetland changes into their component intertidal ecosystem type (tidal flats, tidal marsh or mangroves) and identify when the change occurred (Stage 3).

Machine learning classifiers have been transformative for global-scale models of the distribution of land cover, largely because of their effectiveness at handling large and complex feature sets, ability to be deployed in parallel, and demonstrated high predictive performance across a wide range of applied remote sensing analyses (*36*). They have therefore been used to map the extent of several intertidal ecosystems, including tidal flats (*9*) and mangroves (*13*). For this reason, random forest classifiers were applied at in the three stages of our analysis, using training datasets developed for each and a set of multitemporal data layers as covariates. The models were applied to coastal areas between 60°N and 60°S. To reduce unnecessary analyses within these latitudinal bounds, the analysis was limited to the maximum area represented by the following criteria: less than 40-m water depth (*37*), less than 40-m elevation (*37*), within 5-km of any intertidal ecosystems mapped in existing global-scale maps of single ecosystems (*9, 13, 15, 38, 39*), or less than 5-km to the coastline (*40*). We ran our remote sensing analysis end-to-end in Google Earth Engine (*41*) and used *R* (*42*) to conduct model tuning and develop data summaries. Model code is available as Supplementary Data S1 and the training data and map data products as Supplementary Data S2 and S3.

2. Covariate data

The Landsat Thematic Mapper (TM), Enhanced Thematic Mapper + (ETM+) and Operational Land Imager (OLI) instruments on Landsat 5–8 satellites are amongst the most important data sources for investigating broad-scale dynamics of the Earth's ecosystems (*43-45*). Landsat Collection-1 At-Surface Reflectance data (*46*) were used to produce a set of time-series covariate layers that formed the basis of the three stages of our modelling approach. We collected every Landsat archive image acquired over the study area between 1999 and 2019 (1,166,385 images), masked cloud and cloud shadow pixels (*46*), and summarized them into cloud-free temporal composite metric layers over seven 3-yearly periods (1999–2001, 2002–2004, 2005–2007, 2008–2010, 2011–2013, 2014–2016, 2017–2019). Composite metrics are useful for minimizing contamination by cloud, cloud shadow and snow, characterizing the extent of tidal influence detectable by satellite sensors, and representing diverse aspects of coastal and vegetation dynamics in an efficient manner suitable for use in regional to global-scale classification models (*9, 26, 47, 48*). Analysis time-steps were timed with the launch of the Landsat 7 ETM + instrument and were fixed to three-year periods (*49, 50*). This balanced the requirement for data products of sufficient temporal resolution to investigate intertidal ecosystem dynamics against the need to use a sufficient number of satellite images to generate cloud-free composite metrics across the global intertidal area (*49, 50*). For each three-year time-period, 88 composite metric layers were generated from the Landsat Archive data to serve as spectral covariates in the three classification models. Pixels where a lack of cloud-free observations precluded change classification accounted for only 1.7% of the total mapped area. To promote accurate predictions of the occurrence of tidal wetlands (Stage 1) and their component ecosystem types (Stage 3), we also developed additional covariate layers of biophysical variables known to influence local and global distributions of tidal wetlands (*9, 28, 51, 52*), including air

temperature and elevation. The complete list of covariate layers is presented in Supplementary Table S1.

3. Intertidal ecosystem training data

We developed a globally distributed training dataset for modelling the extent of tidal wetlands and their component intertidal ecosystems. This was achieved through visual interpretation of high-resolution satellite images available from Google Earth, Bing Maps and other mapping platforms (such as Planet Basemaps) in combination with the full set of cloud-free Landsat composite metrics (Table S1). Typically, pixels included in the training set met the following conditions: (i) a clear presence of distinguishing features of each ecosystem type, such as mangrove trees, tidally inundated sediments, or marsh vegetation, (ii) located along the visible natural coastline where intertidal ecosystems are clearly observable, and (iii) the ecosystem was confirmed as present in the reference period (2014–2016). Where possible, other sources of information, including from published studies, coastal atlases and publicly available datasets, were used to aid image interpretation. Image analysts also used their experience and knowledge of the visual characteristics of each ecosystem type to inform their collection of training data and did not include records where there was any uncertainty about the ecosystem type or its presence during the reference period. This resulted in a tidal wetland training dataset of 23,138 occurrence records annotated with ecosystem type (tidal flat, tidal marsh or mangrove). Furthermore, 17,747 occurrence records of non-tidal wetland land cover types were collected to enable separation from other land cover types that occur in the coastal zone (‘permanent water’ and ‘terrestrial other’; Figure S2). The permanent water class included records from deep water and shallow marine ecosystems, including kelp forests, seagrass meadows and photic coral reefs. The terrestrial other class included a variety of land cover types ranging from agriculture and

settlements to sandy shorelines and supra-littoral coastal ecosystems. Our ground-up compilation of training data, as opposed to the sampling of existing publicly available map products, reduces error propagation among global map products and enables the inclusion of training data from areas that are unmapped in existing global map datasets

3. Distribution of tidal wetlands

The Stage 1 random-forest classification model aimed to estimate the global distribution of tidal wetlands, formulated as the combined distribution of the three intertidal ecosystem types represented in our training set. The 'tidal wetland' category comprised the training data of the three intertidal ecosystems, with the 'permanent water' and 'terrestrial other' records combined and used as absence data. The covariate layers (Table S1) were sampled for the reference time period (2014–2016) at the location of each record in the training set. We sought to reduce model complexity by removing highly correlated covariates, however, model testing with the training set indicated that lowest out-of-bag error rates were achieved with the full covariate set. Prior to deploying the classification model in Google Earth Engine, model hyper-parameters were optimized by exploring a hypergrid search space with the training set in *R* using the package 'ranger' (*53*). The hypergrid search consisted of 240 simulations with varying parameter values of the number of trees grown, the number of covariates sampled at each split, the fraction of observations sampled at each split, and the minimum node size. Parameter values deployed in Earth Engine across the full global study area were the mean of the top ten models identified by lowest out-of-bag error rate in the hypergrid simulation. We predicted the global distribution of tidal wetlands for each of the seven time-periods by running random forests in probability mode, which represents the agreement of random forest decision trees, and yields per-pixel tidal wetland probability layers for each time period (*41*).

Owing to similar inundation dynamics, distinguishing low-elevation coastal aquaculture from coastal ecosystems remains a key challenge of coastal remote sensing. Initial model runs indicated commission error with coastal aquaculture, particularly in Java and Vietnam. For this reason, we developed a mask of South-east Asian aquaculture using maps developed of this land cover type for the start year of our analysis in 1999 (*54*). Commission error was also reduced by using the global training set to estimate the ecosystem type of each tidal wetland pixel above 10-m elevation (*52*), corresponding to the maximum elevation of these ecosystems in our training set, masking those estimated as tidal marsh or tidal flat, as well as pixels identified as mangroves that occurred outside of the mangrove habitat layer developed by Global Mangrove Watch program (*13*). After applying these masks, tidal wetland extent maps were obtained by applying a threshold of 0.5 to the tidal wetland probability layers and then post-processed to a minimum mapping unit of 10 eight-way connected 30×30-m pixels.

5. Tidal wetland change product

The overarching aim of our study was to investigate global tidal wetland change over a 20-year period. Although the Stage 1 tidal wetland extent model was designed to deliver extent maps that met stringent quality aspirations, variation in the number of images available per region and known limitations of change maps developed from optical remote sensing can lead to year-on-year variation in mapped extent related to model error and noise, rather than observed changes (*55-58*). We therefore developed a second classification model to classify pixels where image differencing the tidal wetland extent products suggested disturbance events may have occurred during the study period (Stage 2).

We developed an additional global training set for this purpose with a stratified random sample of 950 points in disturbance patches identified by differencing the first (1999–2001) and

last (2017–2019) year of the tidal wetland extent products. We used high-resolution historical imagery from the Google Earth Pro time-slider and the Landsat composite metrics from 1999–2001 and 2017–2019 to annotate each training point according to whether loss, gain or no change was evident over the 20-year study period. Tidal wetland loss was defined as the replacement, at the 30-m pixel scale, of any of the three focal intertidal ecosystems with non-intertidal ecosystems. Tidal wetland gain was defined as the establishment of any of the three intertidal ecosystems in pixels where they did not occur in 1999. According to these definitions, tidal wetland loss and gain training points were included without explicit knowledge of specific change drivers, and therefore included records resulting from diverse change drivers ranging from direct losses due to reclamation, seawalls, dikes, vegetation cutting, mowing, and agricultural development, to die back caused by drivers such as pollution, permanent inundation or altered inundation dynamics. In all cases, pixels labelled as loss indicated a clear loss of defining features of each ecosystem in imagery between the start to the end of the study period while pixels labelled as gain indicated the presence of new intertidal ecosystems that were initially mapped as terrestrial (non-tidal) or permanent open water. Sample pixels where no change was observed were labeled as no change, and any pixels that could not be allocated to a change class due to insufficient historical imagery were excluded from the sample set. Stratified random samples were drawn and assessed in blocks (~500 points), with a sensitivity analysis performed after each block to determine whether the sample size was sufficient to stabilize the overall accuracy estimate. The sensitivity analysis involved a bootstrap resampling approach that simulated an increasing number of validation samples, recording the variance of the accuracy estimate. Similarly to a previous study (*9*), we determined that there were enough validation samples once the variance stabilized such that adding more samples did not significantly change estimates or uncertainty levels. The training set was supplemented over model iterations with

manually acquired samples in areas that represented the most challenging situations of confirmed change. The final training set for the change classifier comprised 1,787 points that represented losses (638 points), gains (457 points) and no change (692 points) of tidal wetlands over the 20 year study period (Figure S3).

For covariates, we computed the difference in pixel values from our Landsat covariate set between the start (1999–2001) and end of the time series (2017–2019; 88 covariates; Table S2). A covariate layer representing the tidal wetland trend was also included by developing a per-pixel linear model fit to the seven per-pixel probability layers of global tidal wetland extent (one covariate; Table S2). We applied the change classification model to all disturbance patches, yielding a global map of pixels depicting losses and gains of tidal wetlands between 1999 and 2019.

To annotate the type of loss or gain, we applied a third random forest classifier to each gain or loss pixel (Stage 3). The intertidal ecosystem type lost or gained was estimated using the covariates for the initial (1999–2001; intertidal ecosystem type in loss patches) and final model time steps (2017–2019; intertidal ecosystem type in gain patches), and the intertidal ecosystem training set (n = 17,772 records). The year of loss or gain ('lossyear' and 'gainyear') was computed as the last or first time-step that a pixel classified as tidal wetland was present in the time series. The change map was post-processed to a minimum mapping unit of 10 eight-way connected 30×30-m pixels and removed obvious classification errors. The final outputs from the analysis were a set of global maps, at 30-m resolution, depicting the estimated global extent of tidal wetlands since 1999, the distribution of tidal wetland losses and gains by intertidal ecosystem type, and the time-step that the loss or gain event was estimated to have occurred (Figure S4).

6. Validation and uncertainty estimates

As noted in many global-scale studies, validation of any land cover maps and their change is extremely challenging (*26, 48*). Errors of omission and commission can arise from model misclassification of dynamic features (e.g., turbid water), insufficient representation of target features in training data, inappropriate formulation of map classification schemes, coarse resolution covariate data that can cause unreliable classifications of features at subpixel scales, and the presence of unmapped features that occur at spatial scales smaller than the minimum mapping unit (*58-60*). We followed convention and employed independent, high spatial resolution satellite data that matched the temporal span of our products to validate the model outputs. Here, we leveraged the growing archive of historical high-resolution imagery available in Google Earth Pro and visualizations of Landsat Archive data to evaluate the accuracy of the tidal wetland extent map (2017–2019) and of the change product (1999–2019). For each validation exercise, we used established practices for assessments of land cover and land cover change to generate validation sets and used these to independently quantify map error and bias of our map products (*57, 59, 61, 62*). We ensured sufficient sample size of the two validation sets with sensitivity analyses to identify the point at which further samples in the validation set would not alter accuracy results outside of a 95% confidence interval (*9, 63*). This process yielded two validation sets developed from stratified random sampling, (i) the extent validation set, consisting of map classes ‘tidal wetland’ and ‘other’ (n =1,359 validation points; Figure S5) and (ii) the change validation set of map classes ‘stable’, ‘gain’ and ‘loss’(n = 3,060 validation points; Figure S6).

To independently annotate validation points in the two validation sets, we developed an online accuracy assessment application in Google Earth Engine (*41*) that enabled an experienced

analyst to concurrently view a relevant set of up to four images for each validation sample. Images available to the analyst included a subset of the time-series Landsat covariates visualized as the Near-Infrared Band, a true color composite, a false color composite, and the standard deviation of the Normalized Difference Water Index (NDWI; *64*), the Modified Normalized Difference Water Index (MNDWI; *65*) and the Automated Water Extraction Index (AWEI; *66*) over the 2017–2019 -year period. The analyst also used Google Earth Pro (including the time-slider function), Bing Maps, and any other information source, including map figures in published papers that enabled an independent assessment of each validation sample.

We used the validation datasets to calculate standard map accuracy metrics, and used newly developed resampling protocols that been shown to be effective for classification analyses of vegetation distributions (*67*) and coastal ecosystem extents (*9*) to estimate map accuracies and confidence intervals. Bootstrapping was performed by resampling the validation samples using 1000 iterations, taking the mean of the sampling distribution as the reported accuracy value and the 0.025 and 0.975 percentiles of the sampling distribution as the 95% confidence interval. Bootstrapping routines yielded accuracy estimates (mean and 95% confidence interval) for the tidal wetland extent and change products (Tables S5-S8).

Traditionally, uncertainty estimates are generated via parametric methods that yield symmetrical confidence intervals around accuracy and area estimates. However, maps derived from remote sensing classifications tend to have uneven omission and commission error due to factors including covariate data quality (such as arising from cloud or smoke haze), sensitivity to tidal dynamics, different spectral similarities among classes, spatiotemporal variation in land cover change, and other uncertainties related to model performance (*57, 58, 61, 62, 67, 68*). Our validation results indicated asymmetry between omission and commission error (Tables S5-S8). To allow propagation of this asymmetry into our estimates of global extent, we used the 95%

interval on the resampled distribution of omission and commission errors to estimate the upper and lower bounds for the area estimates of the tidal wetland class, such that:

$$area_i\ \mathbf{95\%}\boldsymbol{CI}_{lower} = area_i - (area_i * \ commission\ \boldsymbol{P}_{95}\ )$$

$$area_i\ \mathbf{95\%}\boldsymbol{CI}_{upper} = area_i + (area_i * omission\ \boldsymbol{P}_{95})$$

where $area_i$ is the mapped area value for the tidal wetland class *i*, and $\boldsymbol{P}_{95}$ is the 95% percentile of the commission/omission error corresponding to tidal wetland class *i*. Calculating confidence intervals in this manner can result in uneven intervals, but this is a more objective representation of uncertainty for end-users given known asymmetry in commission and omission errors in the map products.

We calculated confidence intervals for the loss and gain estimates for each intertidal ecosystem class using a similar approach, except that the error was multiplicative between the ecosystem class and the change class. For loss estimates,

$$loss_i\ \mathbf{95\%}\boldsymbol{CI}_{lower} = loss_i - \left(loss_i * \ lower_{i,loss}\right)$$

$$loss_i\ \mathbf{95\%}\boldsymbol{CI}_{upper} = loss_i + \left(loss_i * \ upper_{i,loss}\right)$$

where $loss_i$ is the mapped area estimate of class *i* (one of mangrove, tidal marsh or tidal flat) intersected with the loss class in the change product, and

$$lower_{i,loss} = \left(1 - \left((1 - \ commission\ \boldsymbol{P}_{95,i}) * (1 - commission\ \boldsymbol{P}_{95,loss})\right)\right)$$

$$upper_{i,loss} = \left(1 - \left((1 - \ omission\ \boldsymbol{P}_{95,i}) * (1 - commission\ \boldsymbol{P}_{95,loss})\right)\right)$$

where $\boldsymbol{P}_{95,i}$ is the 95th percentile of the commission/omission error for the intertidal ecosystem class *i*, and $\boldsymbol{P}_{95,loss}$ is the 95th percentile of the commission error for the loss class in the change product. The same process was applied for the gain estimates (i.e., replacing loss with gain above). Although this approach considerably widens confidence intervals in derived area estimates, particularly for change estimates of individual ecosystem types, it reflects the dynamic nature of tidal wetlands and the complexities of detecting their change.

7. Tidal wetland analysis.

We estimated the area of the tidal wetland extent and change products and summarized the results at several spatial scales, including global, continental, by country (*69*) (Table S3), and for particular regions of interest, such as the world's 100 largest deltas (*19*) and marine ecoregions (*70*). To investigate the extent of transitions among ecosystems, we also estimated the area of tidal wetlands that changed from one ecosystem type to another (e.g., from tidal flat to mangrove) over the study period (1999–2019). For example, a pixel within the tidal wetland extent map estimated as tidal flat in 1999 but mapped as mangrove in 2019 was flagged as a tidal flat to mangrove transition (Table S4). Only pixels that were mapped as tidal wetlands at the start and end of the study periods (i.e., not lost or gained over the 20 year period) were considered to be transition pixels.

8. Direct and indirect driver analysis

The causes of tidal wetland change are complex and are often the result of synergistic, interacting and/or multiplicative processes that operate at a range of spatial scales. Several studies have attempted to attribute the conversion of mangroves to other land cover types to anthropogenic (human-driven) and natural drivers (*14, 71*). Anthropogenic drivers are typically related to direct human activities (including conversion to aquaculture and other

commodities, urban land uses and infrastructure development). Natural drivers typically include erosion, sediment deposition, sea level rise, and other natural coastal processes, which may be influenced by climate change and remote human-induced land-use changes whose origin may be tens or hundreds of kilometers from the observed change event. These drivers of coastal change operate at local to global scales and complex interactions and synergies are evident worldwide. Disentangling 'natural' and 'anthropogenic' drivers of change is therefore extremely challenging (*72*).

Here we develop a sample-based estimate (*26*) of the relative contribution of direct human activities (such as conversion to aquaculture, agriculture, urban development) and indirect drivers (representing the combined effect of climate change, natural coastal processes, and other remote drivers of change) to the losses and gains of tidal wetlands that were detected by our remote sensing analysis. For this, a global weighted probability sample over the tidal wetland change data was developed to estimate the proportion of direct and indirect drivers on the following tidal wetland change dynamics:

(i) Tidal flat gain;

(ii) Tidal flat loss;

(iii) Tidal marsh gain;

(iv) Tidal marsh loss;

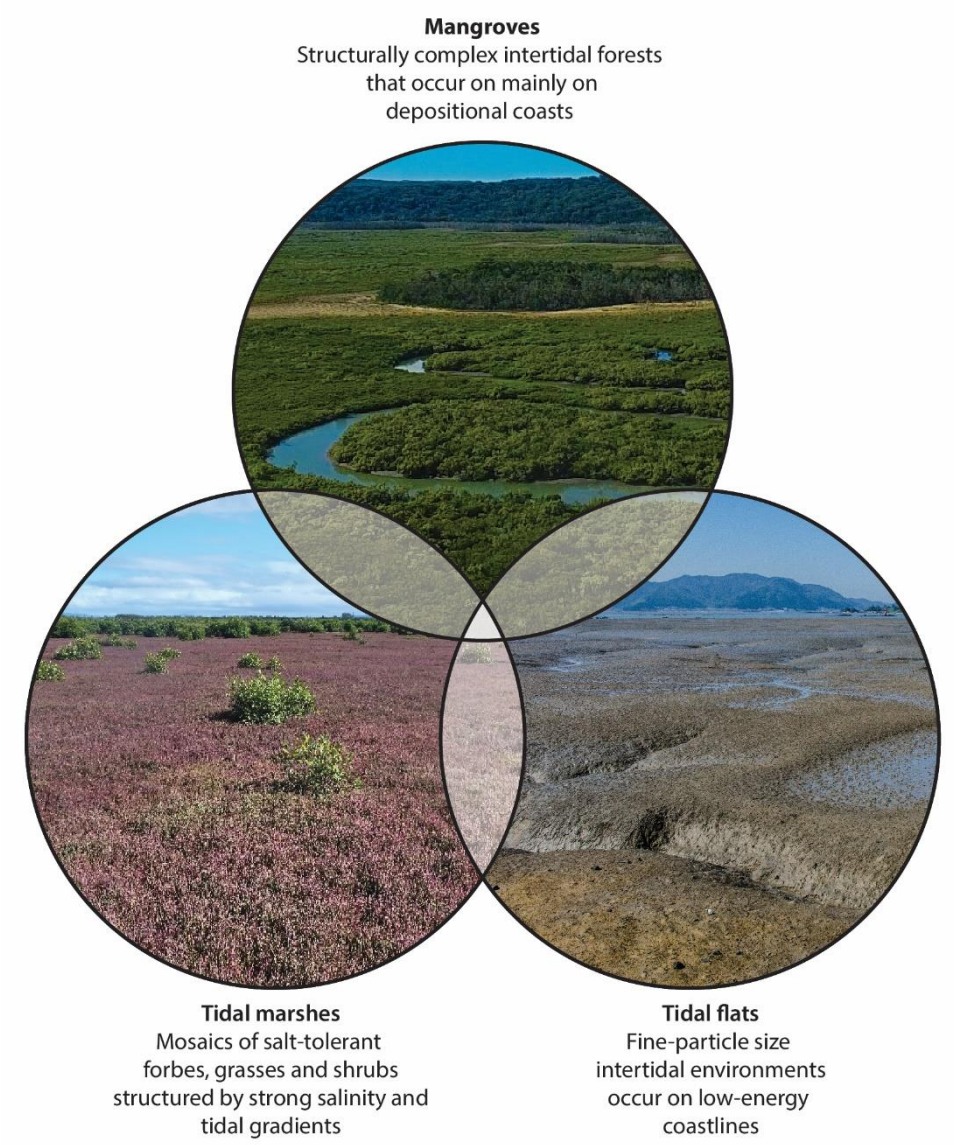
(v) Mangrove gain; and

(vi) Mangrove loss.

For each change dynamic, we sampled 250 3 × 3 kilometer grid cells with a weighted probability proportional to the area of tidal wetland change for the corresponding change dynamic detected within each grid cell. Within each sampled grid cell, we randomly sampled a loss or gain pixel (30-m) that matched the sampled change dynamic of the grid cell (e.g., tidal marsh gain). For each sampled pixel, we created polygon features representing the boundary of the pixel (30-m) for high-resolution image interpretation and an image chip boundary an order of magnitude larger (300-m) for scale reference (Figure S8).

We imported the pixel boundaries into Google Earth Pro and used high-resolution images and the time-slider tool to inspect available high-resolution imagery before, during and after the 1999–2019 study period to assess the drivers of tidal wetland change at the 30-m pixel scale. Changes attributed to direct drivers were associated with visible land changes such as aquaculture, agriculture, plantations, urban and industrial development, and other artificial objects such as coastal infrastructure (bridges and dikes). The impact of indirect drivers was assumed

where samples could not be attributed to a direct driver of change (Figure S8). Samples where clear attribution to the two driver classes was not possible due to lack of imagery or uncertainty about tidal wetland change were removed from the sample set. The relative contribution of direct and indirect drivers of tidal wetland loss and gain were estimated as the proportion of the randomly sampled pixels attributed to the two driver categories.



765 **Figure S1.**

Representative examples of the three intertidal ecosystem types included in the tidal wetland map class.

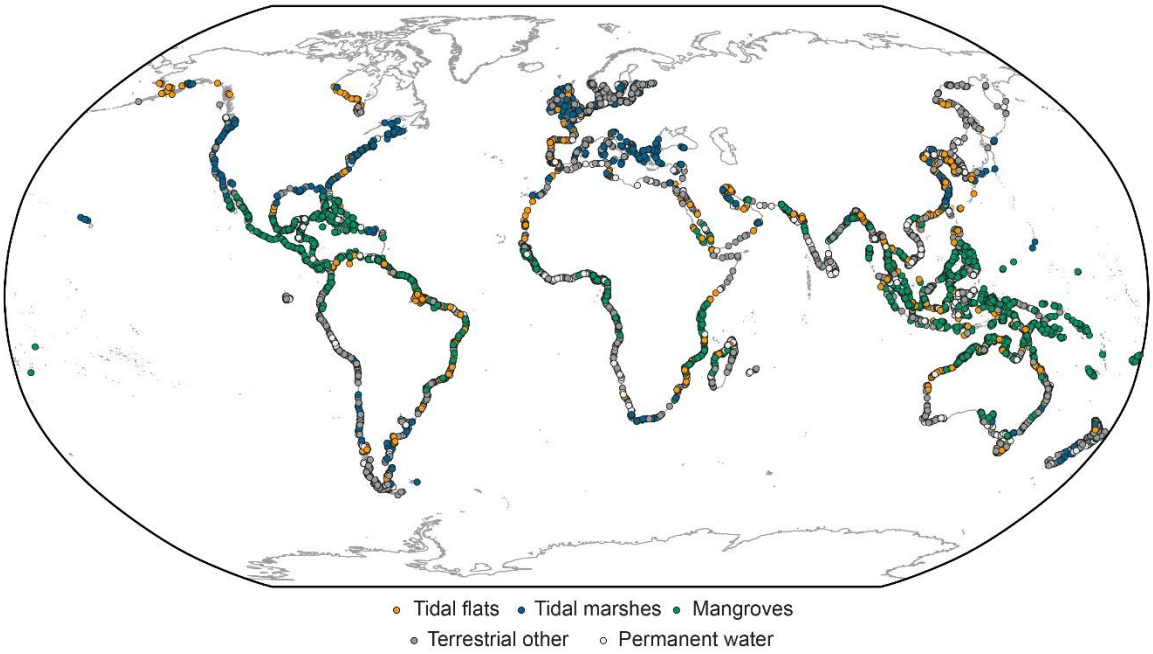


Figure S2.

The global distribution of the training data collected to train the tidal wetlands classification model and classify each pixel to ecosystem type. All training data was collected for the reference period 2014–2016.

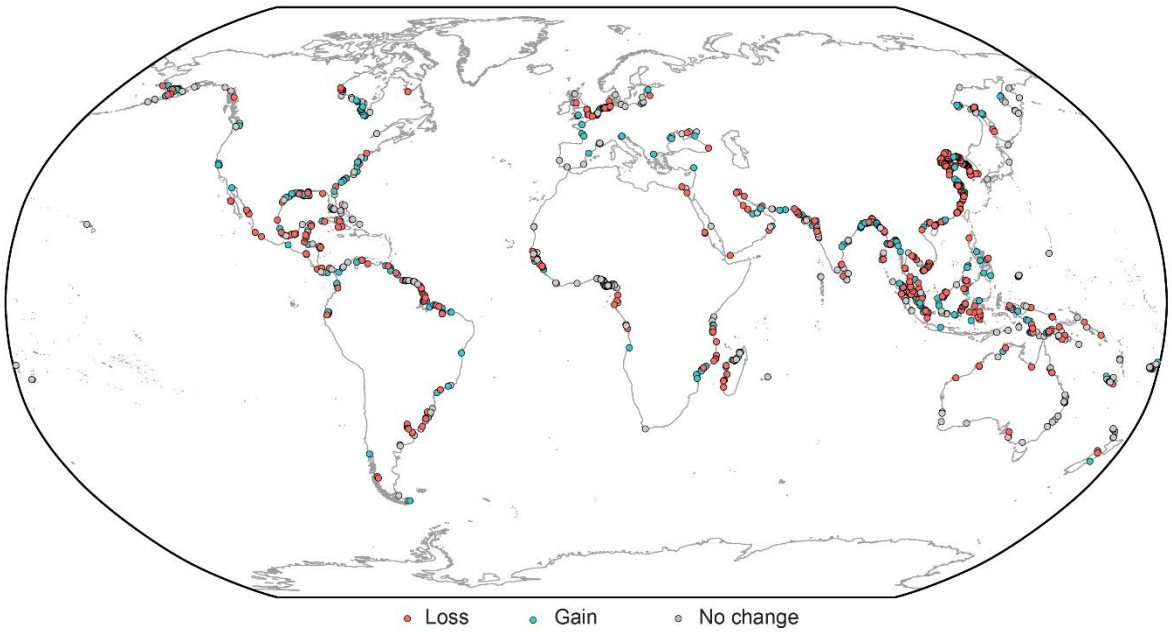


Figure S3.

The global distribution of the training data (n = 1,727) collected to train the global tidal wetland change model for the period 1999–2019.

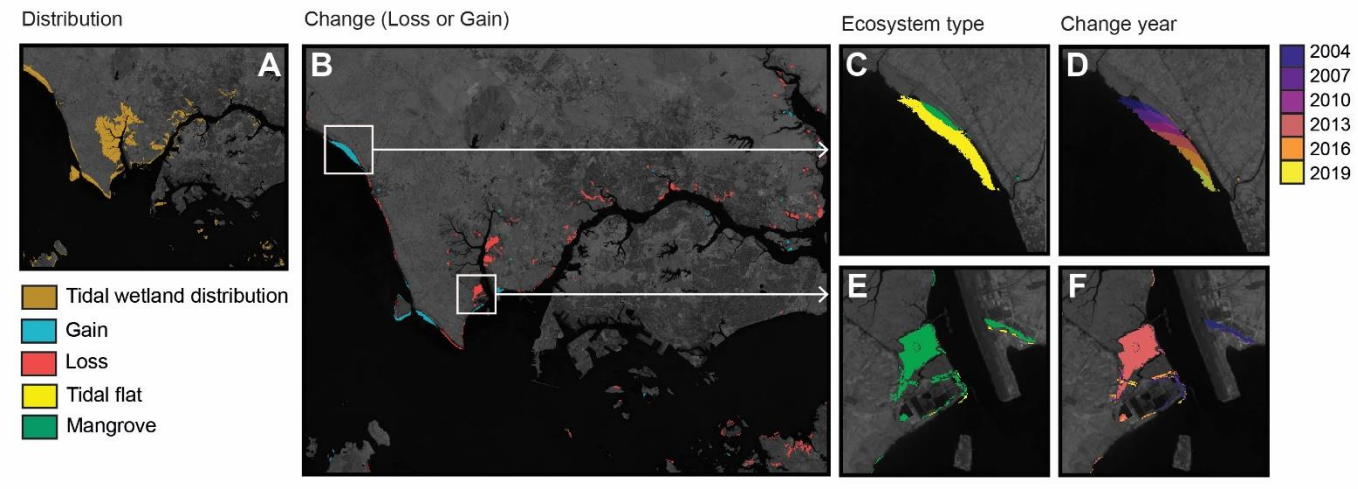


Figure S4.

Example of change detected in tidal wetlands from 1999 to 2019. The figure shows (**A**) the distribution of tidal wetlands (tidal flat, tidal marsh or mangrove) in Malaysia and Singapore, centered at approximately 1.4°N, 103.6°E; (**B**) the loss (red) and gain (blue) data layers. The detailed insets show a new area of tidal wetland caused by sediment deposition, by gain type (**C**) and gain year (**D**); and (**E**) detailed inset of loss by deforestation for an industrial port development, showing loss type (**E**) and loss year (**F**).

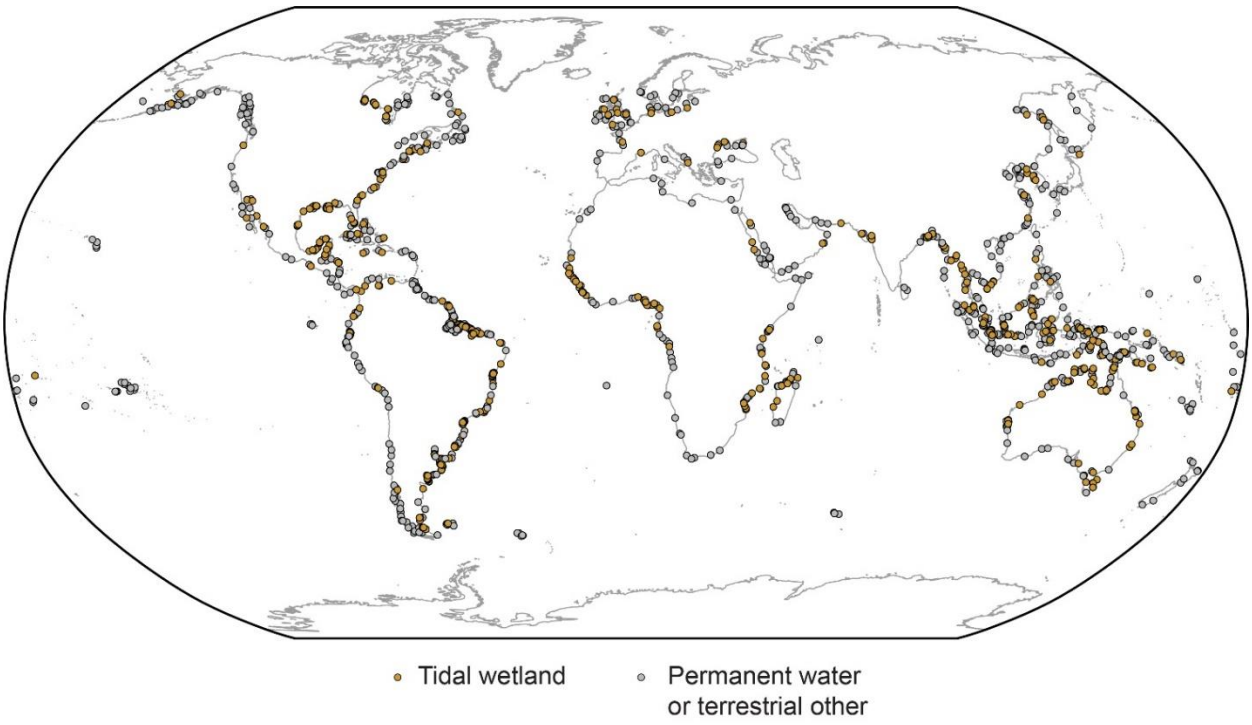


Figure S5.

The validation samples (n = 1359) used to assess the accuracy of the tidal wetland extent product.

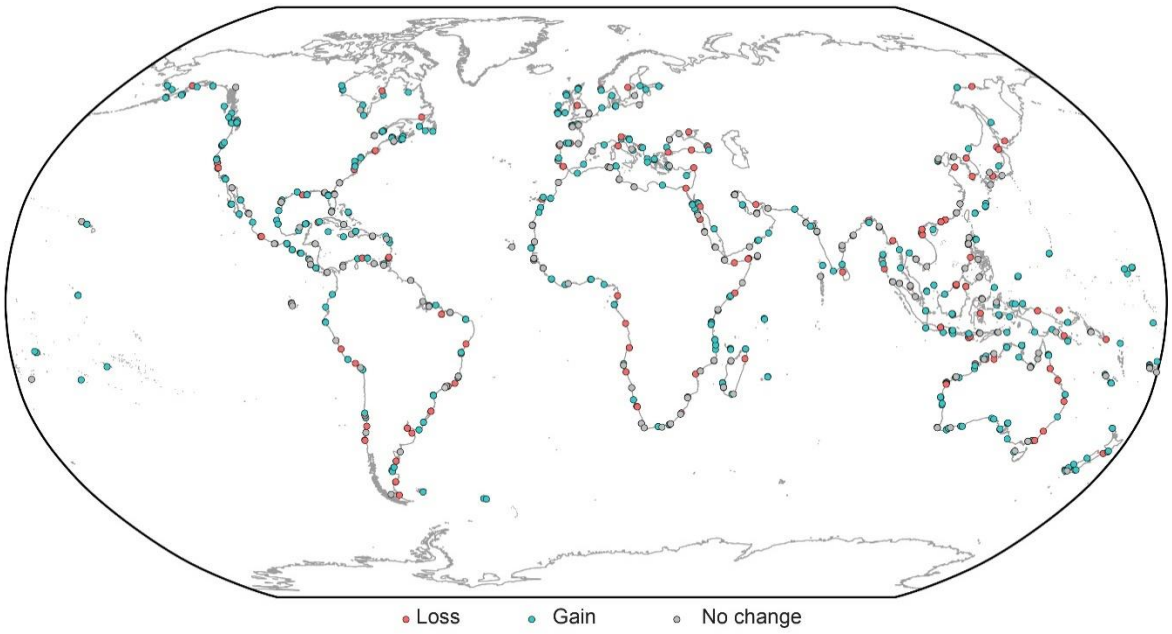


Figure S6.

The validation samples (n = 3060) used to assess the accuracy of the global tidal wetland change product.

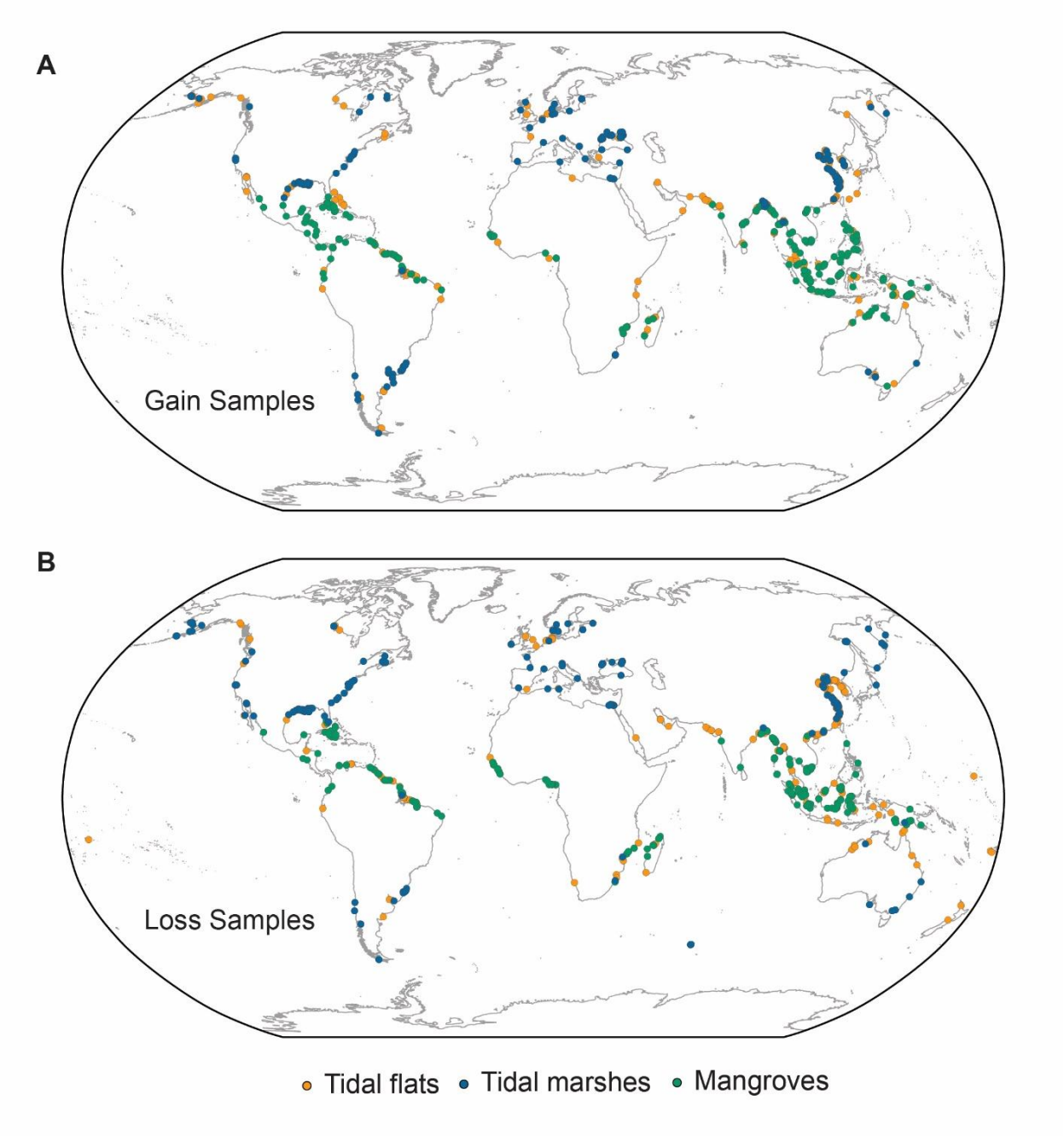


Figure S7.

The driver annotation samples used to assess the relative contribution of direct versus indirect drivers on observed losses and gains of tidal wetlands (n = 1500). The figure shows samples of observed change stratified by ecosystem type for tidal wetland gains (A) and losses (B).

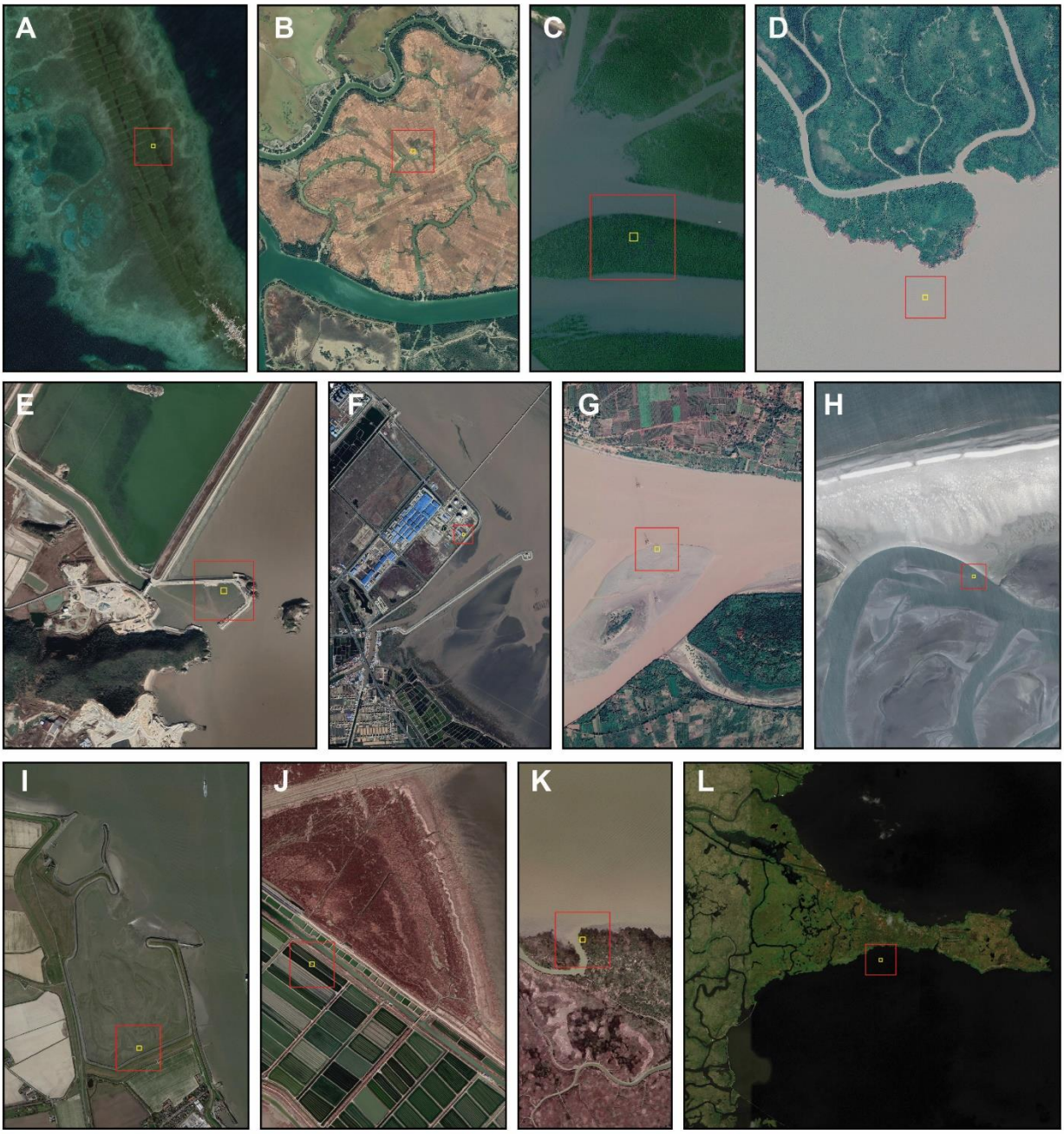


Figure S8.

Examples of direct and indirect drivers of tidal wetland loss and gain. Each row of images from Google Earth Pro indicates an intertidal ecosystem type (mangrove, top; tidal flat, middle; tidal marsh, bottom) and column by direct gain (A, E, I), direct loss (B, F, J), indirect gain (C, G, K) and indirect loss (D, H, L). Yellow squares are 30 x 30-m pixels used to annotate driver type and red squares are 300 x 300-m scale references.

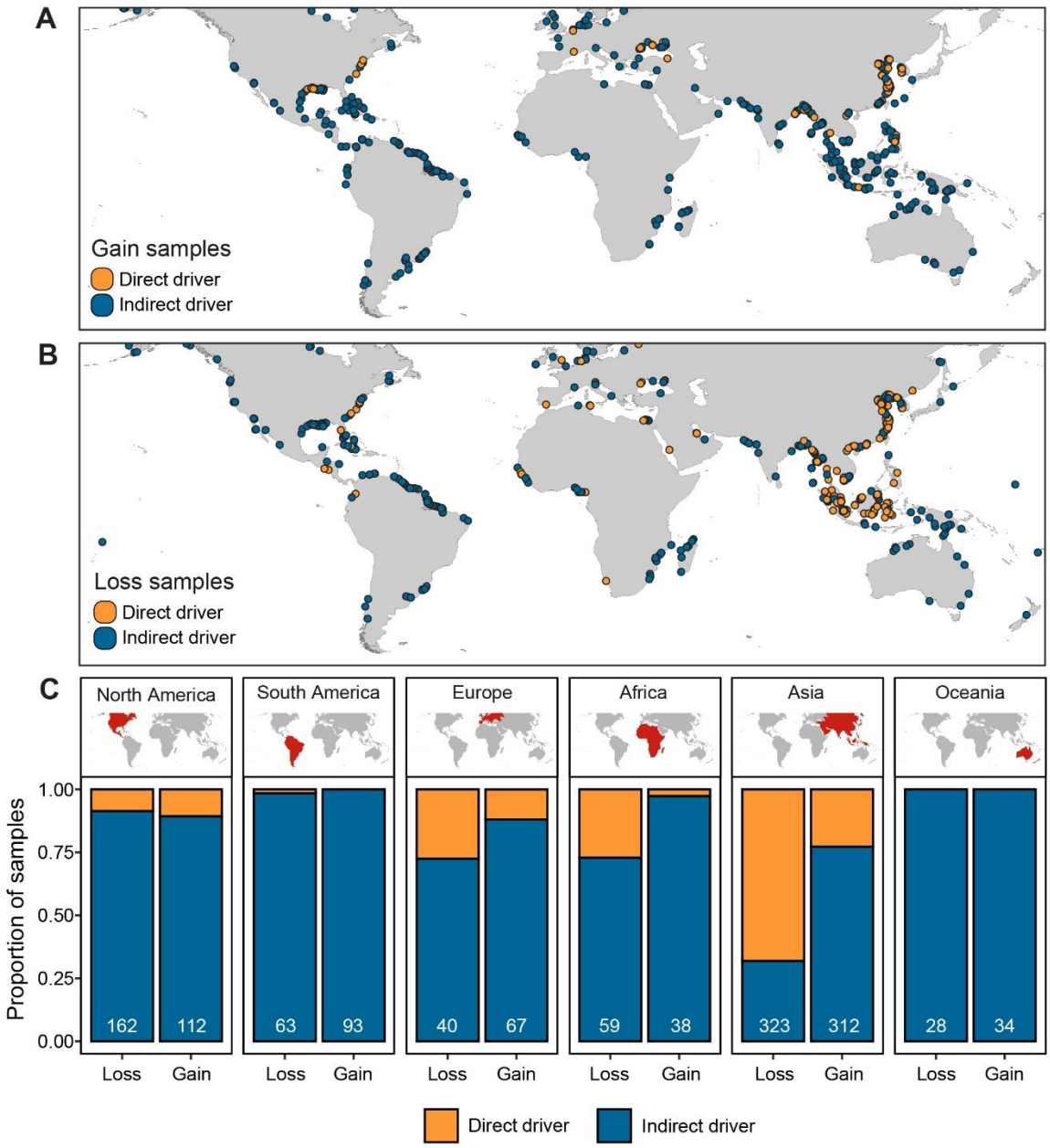


Figure S9.

The contribution of direct and indirect drivers to the observed tidal wetland change. The distribution of the weighted samples used in image interpretation to annotate drivers of gain (A) and loss (B). (C) The proportion of samples attributed to direct and indirect losses per continent. Numbers in each bar indicate the number of samples from the weighted probability sample used to attribute drivers of change.

Table S1.

Datasets used in the global intertidal extent classification models. Each random forest model used per-pixel information from these covariate layers to classify each pixel as tidal wetland or not and change pixels as mangrove, tidal marsh or tidal flats. Four variables in the classification models were static across all years of the time series (elevation, slope, aspect and latitude).

Raw Input Data	Variables	Reducers applied per 3-year period	No. covariate layers per time period	Produced for each time period	Source (web link)
ALOS World 3D - 30m version 2.2 (AW3D30)	Aspect Elevation Slope	N/A	3	No	JAXA[1]
Landsat Collection-1 At-Surface Reflectance	Automated Water Extraction Index (AWEI) Enhanced Vegetation Index (EVI) Modified Normalized Difference Water Index (MNDWI) Normalized Difference Water Index (NDVI) Normalized Difference Water Index (NDWI)	Minimum Maximum Standard Deviation Median 10th Percentile 25th Percentile 50th Percentile 75th Percentile 90th Percentile 0–10 Interval Mean 10–25 Interval Mean 25–50 Interval Mean 50–75 Interval Mean 75–90 Interval Mean 90–100 Interval Mean 10–90 Interval Mean 25–75 Interval Mean	85	Yes	USGS[2]

	Green band Near Infrared band (NIR) Short-wave Infrared band (SWIR)	10–90 Interval Mean	3	Yes	USGS[2]
Latitude	Latitude	N/A	1	No	Developed by authors in Earth Engine
Minimum Temperature (ERA5 ECMWF)	Minimum Temperature	Minimum	1	Yes	Copernicus Climate Data Store[3]

[1] http://www.eorc.jaxa.jp/ALOS/en/aw3d30/

[2] https://www.usgs.gov/media/files/landsat-collection-1-level-1-product-definition

[3] https://cds.climate.copernicus.eu/cdsapp#!/dataset/reanalysis-era5-single-levels

Table S2.

Covariate data inputs used in the tidal wetland change random forest classification model.

Raw Input Data	Variables	Reducers applied per 3-year period	Processing for change analysis	No. covariate layers in intertidal ecosystem change classification model
Linear trend of tidal wetland probability layers (representing agreement among random forest trees for binary tidal wetland class)	Random forest probability layer of tidal wetland extent (result of Stage 1 analysis)	N/A	Per-pixel linear model of 7 time-series random forest probability layers	1
Landsat Collection-1 At-Surface Reflectance	Automated Water Extraction Index (AWEI) Enhanced Vegetation Index (EVI) Modified Normalized Difference Water Index (MNDWI) Normalized Difference Water Index (NDVI) Normalized Difference Water Index (NDWI)	Minimum Maximum Standard Deviation Median 10th Percentile 25th Percentile 50th Percentile 75th Percentile 90th Percentile 0–10 Interval Mean 10–25 Interval Mean 25–50 Interval Mean 50–75 Interval Mean 75–90 Interval Mean 90–100 Interval Mean 10–90 Interval Mean 25–75 Interval Mean	Difference between 1999-2001 and 2017-2019 pixel values	85
	Green band Near Infrared band (NIR) Short-wave Infrared band (SWIR)	10–90 Interval Mean	Difference between 1999-2001 and 2017-2019 pixel values	3

Table S3.

Global, continental and national summaries of tidal wetland loss and gain between 1999 and 2019. Note that only countries that contribute ≥ 0.1% of global net change are included in this table.

Unit	Loss area (km^2)	Gain area (km^2)	Net change (km^2)	Total tidal wetland change area (km^2)	Contribution to global net change (%)	Loss to Gain Ratio
GLOBAL	-13656	9698	-3958	23355	100	1.4
ASIA	-7836	4905	-2931	12741	74.1	1.6
NORTH AMERICA	-1512	1103	-409	2615	10.3	1.4
AFRICA	-1075	684	-390	1759	9.9	1.6
SOUTH AMERICA	-1777	1493	-284	3269	7.2	1.2
OCEANIA	-720	563	-157	1283	4	1.3
EUROPE	-737	951	214	1688	-5.4	0.8
Indonesia, Republic of	-2198	772	-1426	2970	36	2.9
China, People's Republic of	-2246	1433	-813	3679	20.6	1.6
Myanmar, Union of	-896	421	-475	1317	12	2.1
Brazil, Federative Republic of	-1140	828	-312	1969	7.9	1.4
Vietnam, Socialist Republic of	-347	144	-203	490	5.1	2.4
Cuba, Republic of	-264	70	-193	334	4.9	3.8
United States of America	-843	668	-174	1511	4.4	1.3
Nigeria, Federal Republic of	-185	27	-158	212	4	6.9
Malaysia	-290	148	-142	437	3.6	2
Guinea, Republic of	-93	22	-70	115	1.8	4.1
Papua New Guinea, Independent State of	-214	148	-66	363	1.7	1.4
Korea, Democratic People's Republic of	-129	79	-50	208	1.3	1.6
Guyana, Co-operative Republic of	-92	45	-47	137	1.2	2
Marshall Islands, Republic of the	-42	1	-41	43	1	41.8
Bahamas, Commonwealth of the	-67	32	-35	99	0.9	2.1
Ghana, Republic of	-34	3	-32	37	0.8	13
Saudi Arabia, Kingdom of	-36	7	-29	43	0.7	4.8
Mozambique, Republic of	-202	176	-26	378	0.7	1.1
Thailand, Kingdom of	-89	64	-24	153	0.6	1.4
Guinea-Bissau, Republic of	-85	61	-24	146	0.6	1.4
Australia, Commonwealth of	-380	357	-23	737	0.6	1.1
Colombia, Republic of	-135	113	-22	249	0.6	1.2
Qatar, State of	-22	1	-22	23	0.5	38.6
Sierra Leone, Republic of	-22	2	-20	24	0.5	8.9
Madagascar, Republic of	-217	198	-19	414	0.5	1.1
Pakistan, Islamic Republic of	-97	79	-18	176	0.5	1.2

New Zealand	-47	30	-17	76	0.4	1.6
Nicaragua, Republic of	-34	19	-15	54	0.4	1.8
Egypt, Arab Republic of	-77	63	-13	140	0.3	1.2
Tunisia, Tunisian Republic	-20	7	-13	27	0.3	2.7
South Africa, Republic of	-32	21	-11	53	0.3	1.6
Cambodia, Kingdom of	-16	6	-10	22	0.3	2.6
Bahrain, Kingdom of	-9	0	-9	9	0.2	25.2
Honduras, Republic of	-24	15	-8	39	0.2	1.5
Samoa, Independent State of	-7	0	-7	8	0.2	33
Peru, Republic of	-20	14	-7	34	0.2	1.5
Somalia, Somali Republic	-7	2	-6	9	0.1	4.8
Italy, Italian Republic	-20	14	-6	34	0.1	1.4
Brunei Darussalam	-6	1	-5	7	0.1	8.2
Fiji, Republic of the Fiji Islands	-13	7	-5	20	0.1	1.7
Gabon, Gabonese Republic	-9	4	-5	13	0.1	2
Belize	-11	7	-4	18	0.1	1.7
Jamaica	-6	2	-4	8	0.1	2.6
Sweden, Kingdom of	-5	1	-4	6	0.1	4.1
Cameroon, Republic of	-12	9	-4	21	0.1	1.4
Liberia, Republic of	-4	1	-3	4	0.1	6.7
Iraq, Republic of	-5	2	-3	7	0.1	2.3
Haiti, Republic of	-10	7	-3	17	0.1	1.4
Dominican Republic	-6	8	2	13	-0.1	0.7
Trinidad and Tobago, Republic of	-1	4	2	5	-0.1	0.4
Libyan Arab Jamahiriya	-3	5	2	8	-0.1	0.6
Kiribati, Republic of	0	3	2	3	-0.1	0.2
Ireland	-11	14	2	25	-0.1	0.8
Japan	-25	28	3	53	-0.1	0.9
Mauritania, Islamic Republic of	-1	4	3	6	-0.1	0.3
Taiwan	-7	10	3	17	-0.1	0.7
Turkey, Republic of	-31	34	3	65	-0.1	0.9
Montenegro, Republic of	-1	5	3	6	-0.1	0.3
Costa Rica, Republic of	-10	13	4	23	-0.1	0.7
Mexico, United Mexican States	-205	210	4	415	-0.1	1
Ecuador, Republic of	-34	39	6	73	-0.1	0.9
Kuwait, State of	-6	14	7	20	-0.2	0.5
Cyprus, Republic of	0	9	8	9	-0.2	0
France, French Republic	-168	178	9	346	-0.2	0.9
Korea, Republic of	-121	133	12	255	-0.3	0.9
Tanzania, United Republic of	-27	40	13	67	-0.3	0.7
Netherlands, Kingdom of the	-61	75	14	136	-0.4	0.8
Panama, Republic of	-21	38	16	59	-0.4	0.6

United Kingdom of Great Britain & Northern Ireland	-124	146	22	270	-0.6	0.8
Venezuela, Bolivarian Republic of	-129	154	25	282	-0.6	0.8
Romania	-6	31	25	38	-0.6	0.2
Ukraine	-25	51	27	76	-0.7	0.5
Suriname, Republic of	-101	135	35	236	-0.9	0.7
Argentina, Argentine Republic	-89	125	37	214	-0.9	0.7
Russian Federation	-225	274	49	500	-1.2	0.8
Germany, Federal Republic of	-120	212	92	332	-2.3	0.6
Bangladesh, People's Republic of	-595	709	114	1304	-2.9	0.8
Philippines, Republic of the	-80	208	128	287	-3.2	0.4

850

Table S4.

Summary of tidal wetland pixels that transitioned from one intertidal ecosystem type to another between 1999 and 2019.

Transition Type	Area (km^2)	Percent of total transition area (%)
Tidal marsh to tidal flat	643.0	9.7
Tidal marsh to mangrove	910.3	13.7
Tidal flat to tidal marsh	1902.1	28.6
Tidal flat to mangrove	1779.4	26.7
Mangrove to tidal flat	552.2	8.3
Mangrove to tidal marsh	865.2	13.0
Total transition pixels	**6652.3**	**100.0**

Table S5.

Class accuracy results for the global tidal wetland classification model based on validation sample points over the mapped area (n = 1359).

		Reference	
		Other	**Tidal wetland**
Mapped	**Other**	673	8
	Tidal wetland	191	487

Table S6.

Quantitative accuracy assessment results for the global tidal wetland classification model based on validation sample points over the mapped area (n = 1359). Quantitative accuracy assessments involved bootstrapping the validation samples (n = 1000 iterations), with the mean of the sampling distribution as the reported accuracy estimate and the 0.025 and 0.975 percentiles of the sampling distribution as the 95% confidence interval.

Error	Estimate	95% Confidence Interval	
		Lower	Upper
Overall accuracy	0.854	0.836	0.871
Other (commission)	0.988	0.979	0.996
Other (omission)	0.779	0.758	0.801
Tidal wetland (commission)	0.719	0.684	0.754
Tidal wetland (omission)	0.984	0.972	0.994

Table S7.

Class accuracy results for the global intertidal change classification model based on validation sample points over the mapped area (n = 3059).

		Reference		
		Loss	**Stable**	**Gain**
Mapped	**Loss**	143	65	11
	Stable	26	477	107
	Gain	6	57	86

Table S8.

Quantitative accuracy assessment results for the global intertidal change classification model based on validation sample points over the mapped area (n = 3059). Quantitative accuracy assessments involved bootstrapping the validation samples (n = 1000 iterations), with the mean of the sampling distribution as the reported accuracy estimate and the 0.025 and 0.975 percentiles of the sampling distribution as the 95% confidence interval.

Error	Estimate	95% Confidence Interval	
		Lower	Upper
Overall accuracy	0.722	0.696	0.751
Loss (commission)	0.652	0.589	0.712
Loss (omission)	0.817	0.766	0.871
No change (commission)	0.782	0.748	0.815
No change (omission)	0.796	0.773	0.820
Gain (commission)	0.579	0.503	0.658
Gain (omission)	0.423	0.374	0.473

Table S9.

The proportion of observed tidal wetland changes attributed to direct drivers at the 30-m pixel scale. Each random sample of tidal wetland change was assessed using high-resolution time-series images available in Google Earth Pro. Direct drivers included changes due to land changes such as aquaculture, agriculture, plantations, urban and industrial development, and other artificial objects such as coastal infrastructure (bridges and dikes). Indirect drivers of change were not directly observable in high-resolution time-series images and include the effects of natural coastal processes, climate change, and remote drivers of change such as change in catchment sediment flux. Samples that could not be allocated to a direct or indirect driver due to lack of high-resolution imagery or uncertainty about tidal wetland change were excluded from the analysis.

Change type	No. Direct	No. Indirect	SE	Direct (%)	n (sampled)	n (excluded)	n (annotated)
Mangrove gain	17	208	3.964	8	250	25	225
Mangrove loss	110	110	7.416	50	250	30	220
Tidal marsh gain	68	155	6.875	30	250	27	223
Tidal marsh loss	47	169	6.064	22	250	34	216
Tidal flat gain	7	201	2.601	3	250	42	208
Tidal flat loss	105	134	7.673	44	250	11	239
TIDAL WETLAND GAIN	92	564	8.894	14	750	94	656
TIDAL WETLAND LOSS	262	413	12.661	39	750	75	675

Table S10.

Attribution of observed changes to direct or indirect drivers by continent. The contribution of direct and indirect drivers was estimated as the proportion of a global weighted probability sample of observed changes to the direct driver class (% direct).

Continent	Tidal wetland		Mangrove		Tidal marsh		Tidal flats	
	Loss (% direct)	Gain (% direct)	Loss (% direct)	Gain (% direct)	Loss (% direct)	Gain (% direct)	Loss (% direct)	Gain (% direct)
Africa	27	3	20	5	50	0	15	0
Asia	68	23	75	13	69	59	62	5
Europe	28	12	0	0	38	17	7	5
North America	9	11	18	0	8	19	0	4
Oceania	0	0	0	0	0	0	0	0
South America	2	0	3	0	0	0	0	0